MuSCAT2: four-color simultaneous camera for the 1.52-m Telescopio Carlos Sánchez

Norio Narita
Akihiko Fukui
Nobuhiko Kusakabe
Noriharu Watanabe
Enric Palle
Hannu Parviainen
Pilar Montañés-Rodríguez
Felipe Murgas
Matteo Monelli
Marta Aguiar
Jorge Andres Perez Prieto
Álex Oscoz
Jerome de Leon
Mayuko Mori
Motohide Tamura
Tomoyasu Yamamuro
Victor J. S. Béjar
Nicolas Crouzet
Diego Hidalgo
Peter Klagyivik
Rafael Luque
Taku Nishiumi

SPIE.

MuSCAT2: four-color simultaneous camera for the 1.52-m Telescopio Carlos Sánchez

Norio Narita,[a,b,c,d,e,*] Akihiko Fukui,[e,f,g] Nobuhiko Kusakabe,[b,d] Noriharu Watanabe,[d,h] Enric Palle,[e,i]
Hannu Parviainen,[e,i] Pilar Montañés-Rodríguez,[e,i] Felipe Murgas,[e,i] Matteo Monelli,[e,i] Marta Aguiar,[e]
Jorge Andres Perez Prieto,[e,i] Álex Oscoz,[e,i] Jerome de Leon,[a] Mayuko Mori,[a] Motohide Tamura,[a,b,d]
Tomoyasu Yamamuro,[j] Victor J. S. Béjar,[e,i] Nicolas Crouzet,[e,i] Diego Hidalgo,[e,i] Peter Klagyivik,[e,i]
Rafael Luque,[e,i] and Taku Nishiumi[k]
[a]The University of Tokyo, Department of Astronomy, Tokyo, Japan
[b]Astrobiology Center, Tokyo, Japan
[c]Japan Science and Technology Agency, PRESTO, Tokyo, Japan
[d]National Astronomical Observatory of Japan, Tokyo, Japan
[e]Instituto de Astrofísica de Canarias (IAC), Tenerife, Spain
[f]The University of Tokyo, Department of Earth and Planetary Science, Tokyo, Japan
[g]Subaru Telescope Okayama Branch Office, National Astronomical Observatory of Japan, Okayama, Japan
[h]SOKENDAI (The Graduate University of Advanced Studies), Tokyo, Japan
[i]Universidad de La Laguna (ULL), Departamento de Astrofísica, Tenerife, Spain
[j]OptCraft, Kanagawa, Japan
[k]Kyoto Sangyo University, Department of Physics, Kyoto, Japan

Abstract. We report the development of a four-color simultaneous camera for the 1.52-m Telescopio Carlos Sánchez in the Teide Observatory, Canaries, Spain. The instrument, named MuSCAT2, has a capability of four-color simultaneous imaging in g (400 to 550 nm), r (550 to 700 nm), i (700 to 820 nm), and z_s (820 to 920 nm) bands. MuSCAT2 equips four 1024×1024 pixel CCDs, having a field of view of 7.4×7.4 arc min^2 with a pixel scale of 0.44 arc sec per pixel. The principal purpose of MuSCAT2 is to perform high-precision multicolor exoplanet transit photometry. We demonstrate photometric precisions of 0.057%, 0.050%, 0.060%, and 0.076% as root-mean-square residuals of 60 s binning in g, r, i, and z_s bands, respectively, for a G0 V star WASP-12 ($V = 11.57 \pm 0.16$). MuSCAT2 has started science operations since January 2018, with over 250 telescope nights per year. MuSCAT2 is expected to become a reference tool for exoplanet transit observations and substantially contributes to the follow-up of the Transiting Exoplanet Survey Satellite and Planetary Transits and Oscillations of stars space missions. © The Authors. Published by SPIE under a Creative Commons Attribution 3.0 Unported License. Distribution or reproduction of this work in whole or in part requires full attribution of the original publication, including its DOI. [DOI: 10.1117/1.JATIS.5.1 .015001]

Keywords: instrumentation; exoplanets; multicolor; photometry; transits.

Paper 18049 received Jul. 4, 2018; accepted for publication Nov. 26, 2018; published online Dec. 27, 2018.

1 Introduction

Transiting planets, periodically passing in front of their host stars, are valuable targets for exoplanet studies since one can investigate the true mass, radius, density, orbital obliquity, and atmosphere of such planets. The number of discovered transiting planets is drastically increasing in recent years thanks to intense transit surveys from the ground[1–6] and space.[7–9] Moreover, the NASA mission Transiting Exoplanet Survey Satellite (TESS)[10] has started operations in 2018, and the future ESA mission Planetary Transits and Oscillations of stars (PLATO)[11] is planned to be launched around 2026. Those missions will especially focus on relatively bright nearby planet host stars. Hence, it is expected that hundreds or thousands of transiting planets, suitable for further characterizations, will be discovered in the vicinity of our Solar system in the near future.

On the other hand, discovered candidates of transiting planets are not always *bona fide* planets. This is because eclipsing binaries may mimic transit-like signals in photometric survey data. False positive rates are especially worse for ground-based surveys (e.g., >98% for the recent KELT survey[12]) and still not negligible even for a space-based survey, such as Kepler.[13] This is also true for the upcoming TESS mission, and the false positive rate is predicted as 30% to 70%[14] depending on the galactic latitude. Thus one needs to distinguish and exclude false positives caused by eclipsing binaries to validate the true planetary nature by additional follow-up observations.

To validate the *bona fide* planetary nature of each candidate, we have focused on the capabilities of multicolor transit photometry. Dimming caused by a true planet should be fairly achromatic, whereas that caused by an eclipsing binary would change significantly with wavelength. We previously developed a multicolor simultaneous camera named MuSCAT[15] for the 1.88-m telescope of National Astronomical Observatory of Japan located in Okayama, Japan, which is capable of three-color simultaneous imaging in g (400 to 550 nm), r (550 to 700 nm), and z_s (820 to 920 nm) bands. MuSCAT has demonstrated high photometric precisions of <0.05% as root-mean-square (rms) residuals of 60 s binning for a 10th magnitude star HAT-P-14[16] and have successfully validated several transiting planets.[17–19] In the upcoming TESS era, high-precision multicolor transit photometry becomes more important due to the large number of potential candidates of transiting planets. To efficiently validate true transiting planets, it is desired to deploy multiple multicolor simultaneous cameras on 1- to 2-m

class telescopes around the world. We thus decided to develop the second multicolor simultaneous camera for the 1.52-m Telescopio Carlos Sánchez (TCS) in the Teide Observatory, Canaries, Spain, which is located at the longitude difference of about 150 deg from the Okayama observatory.

In addition to the importance for validating true planets, ground-based instruments for high precision transit photometry will become more important in the TESS era due to the following reasons: first, since the pixel scale of TESS is 21 arc sec [10] and a typical aperture size is over 1 arc min, there is a high possibility of blending nearby stars in the same aperture with targets. For this reason, additional transit observations are necessary to identify which star is indeed dimming and to derive precise radii of discovered transiting planets. Second, the monitoring duration of TESS for each sector is only about 27 days, which is significantly shorter than the Kepler (over 4 years) or K2 (about 80 days) missions. Thus, it is very important to observe additional transits after the TESS observations to improve the transit ephemerides of targets. This is especially important for selecting potential JWST targets, as observing times of such space telescopes are quite valuable.[20] Third, for multitransiting planetary systems in mean motion resonance (MMR), such as TRAPPIST-1[5] or K2-19,[21,22] high precision transit observations can determine the masses of the planets via transit timing variations (TTVs). TTVs would become a good alternative method to measure the masses of transiting planets in MMR in the TESS era. Finally, optical transit depths of a true planet surrounded by hydrogen dominated atmosphere have a weak wavelength dependence caused by the nature of the planetary atmosphere.[23–25] High precision multicolor transit photometry is useful to probe such weak wavelength dependence and efficiently select good targets for further follow-up with larger ground-based or space-based telescopes.

The rest of this paper is organized as follows: we first describe the TCS 1.52-m telescope in the Teide Observatory (Sec. 2). We then detail designs of the optical system of MuSCAT2 and characteristics of its components (Sec. 3). We report the performance of MuSCAT2 based on commissioning observations (Sec. 4). We finally summarize this paper (Sec. 5).

2 Carlos Sánchez Telescope

The Carlos Sánchez telescope (latitude: 28° 18′ 01.8″ N, longitude: 16° 30′ 39.2″ W) is located at the Teide Observatory (OT), at 2386.75-m over sea level. The OT is one of the best astronomical observing sites in the world with a typical weather success rate of about 80% and a typical seeing size of about 0.8 arc sec. TCS has a primary mirror with a diameter of 1.52 m (60″). Originally built by Imperial College of Science, Technology, and Medicine in collaboration with other groups from the UK and Instituto de Astrofísica de Canarias (IAC), it was commissioned in 1971 and started operations in 1972. It was originally designed as a low cost flux collector for infrared astronomy and it was one of the earliest telescopes with a thin mirror. For many years, it was one of the largest telescopes in the world mainly settled for infrared astronomy. In 1983 telescope ownership was transferred to the IAC and major improvements in order to keep the telescope in a competitive status were performed, including automating control and data acquisition, development of instrumentation for common use and improving the pointing precision and tracking.

The TCS main mirror is fixed in an equatorial structure with a Cassegrain focus and focal length of $f/13.8$ in a Dall–Kirkham type configuration. Its common user-instrumentation includes two other instruments: CAIN and FastCam. More technical details on the TCS and current instruments can be found at Ref. 26.

3 MuSCAT2 Instrument

3.1 Instrumental Optical Design

The optical layout of MuSCAT2 is shown in Fig. 1. MuSCAT2 is installed at the Cassegrain focus of the TCS as shown in Fig. 2. The optical system of MuSCAT2 is composed of F-conversion lenses (lens-1 and lens-2) to widen the field-of-view (FoV) and dichroic mirrors (DMs) to separate light into four-wavelength bands. The F-conversion lenses are placed before and after the DMs, and play roles to make F-number faster (focal image brighter) and to correct off-axis coma aberration characteristic of a Dall–Kirkham type telescope. The lens-1 roughly corrects off-axis coma aberration of all bands, and converts F-number from $f/13.8$ to $f/8$. The lens-2, which are not identical but optimized for each band, further correct coma aberration of each band and convert F-number from $f/8$ to $f/4.2$. All the lenses are applied antireflection (AR) coating of <1% reflectance ratio. A secondary mirror position is about 34 mm closer from the nominal position to obtain focused images on the detectors of MuSCAT2.

Simulated spot diagrams on CCD cameras of MuSCAT2 are shown in Figs. 3 and 4. Figure 3 plots spot diagrams for on-focus cases. The figure indicates spot radius of all wavelength bands are well <0.5 arc sec throughout the FoV. This means the imaging performance of MuSCAT2 is sufficiently good compared to the typical seeing (0.8 arc sec) of the Teide observatory. Figure 4 does for defocused cases where the secondary mirror is shifted by 5 mm from the focused position, which makes the spot radius expand to 5 to 6 arc sec. The figure implies that images are nearly circular throughout the FoV and suitable for aperture photometry.

3.2 Dichroic Mirrors

Three DMs to separate incoming light into four wavelength channels are manufactured by Asahi Spectra Co., Ltd. The sizes and wedge angles of the DMs are summarized in Table 1. The reflectance of the DMs is shown in Fig. 5 and the DMs transmit remaining lights almost completely due to antireflection coating processed on the back sides of the DMs. All the DMs are inserted with an incident angle of 30 deg. Plain mirrors are placed after DMs for ch. 1, 2, and 3 to optimize mechanical structure.

3.3 Bandpass Filters

Following the experience on MuSCAT, we adopt commercially-available g', r', and z_s band filters of Astrodon Photometrics Generation 2 Sloan filters for ch. 1, 2, and 4, respectively. The three filters are the same with those for MuSCAT on Okayama 1.88-m telescope. On the other hand, since the i' band filter of Astrodon Photometrics Generation 2 Sloan filters has an unavoidable overlap of transparent wavelength with the r' and z_s band filters, we adopt a custom-ordered i band filter manufactured by Asahi Spectra Co., Ltd. For simplicity, hereafter we call those channels as g, r, i, and z_s bands, respectively.
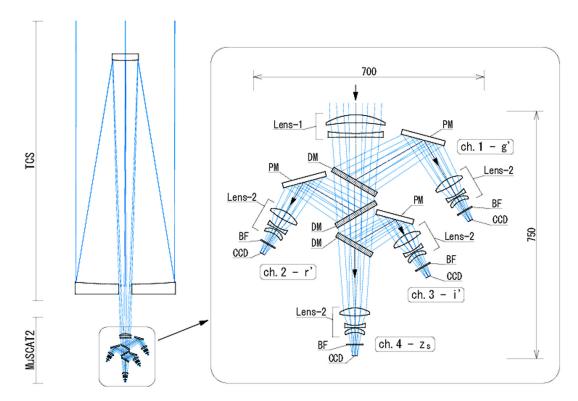
Fig. 1 Layout of the optical system of TCS and MuSCAT2. The left side shows ray trace for the whole telescope and instrument system. The right side is an enlarged view of ray trace for MuSCAT2. Incident light is separated into four channels by three DMs. F-conversion lenses are placed before (lens-1) and after (lens-2) the DMs. Plane mirrors (PMs) are inserted in the channels 1 to 3 to fold optical path. Bandpass filters (BFs) are inserted just before the CCD cameras. Instrument sizes are described in millimeter.

We note that the reflectance and transmittance of the DMs are optimized for those four bandpass filters. The size of those filters is 50 mm × 50 mm. Figure 6 plots the measured transmittance of the bandpass filters.

Fig. 2 A picture of MuSCAT2 installed at the Cassegrain focus of the TCS 1.52-m telescope. The orientation of the picture corresponds to the right side of Fig. 1.

3.4 CCD Cameras

MuSCAT2 equips four CCD cameras manufactured by Princeton Instruments: one is PIXIS: 1024B used for the ch. 2 (r band), and the others are PIXIS: 1024B_eXcelon used for the other three channels (g, i, and z_s bands). Each PIXIS camera equips an e2v 47-10 advanced inverted mode operation science grade 1 CCD. The cosmetic quality of the CCD is very high. The CCD specification declares there are <200 bad pixels among 10^6 pixels and there is no column defect. Basic specifications (e.g., size, weight, etc.) of those CCD cameras are identical with MuSCAT on the Okayama 188 cm telescope (Table 1 of the paper for MuSCAT[15]). Individual characteristics such as values of dark current and readout noise are summarized in Table 2, measured by the manufacturer as inspection verification. Total transmittance of the MuSCAT2 instrument, including all the optics and the quantum efficiency of the detectors, is plotted in Fig. 7. Each CCD camera is independently controllable from an instrument operating PC so that observers can set either individually-different exposure times or synchronized ones, depending on science cases. Typical time interval between two exposures due to readout and fits file creation is 1 to 4 s. Engineering test results for (non-)linearity and saturation level of the individual CCDs are shown in Sec. 4.3.

3.5 Instrument Rotator

As the TCS is not equipped with an instrument rotator at the Cassegrain focus, we installed a custom-made instrument rotator between the telescope flange and MuSCAT2. The reason why the instrument rotator is attached is that it is important to obtain good comparison stars in the field of view to enable high
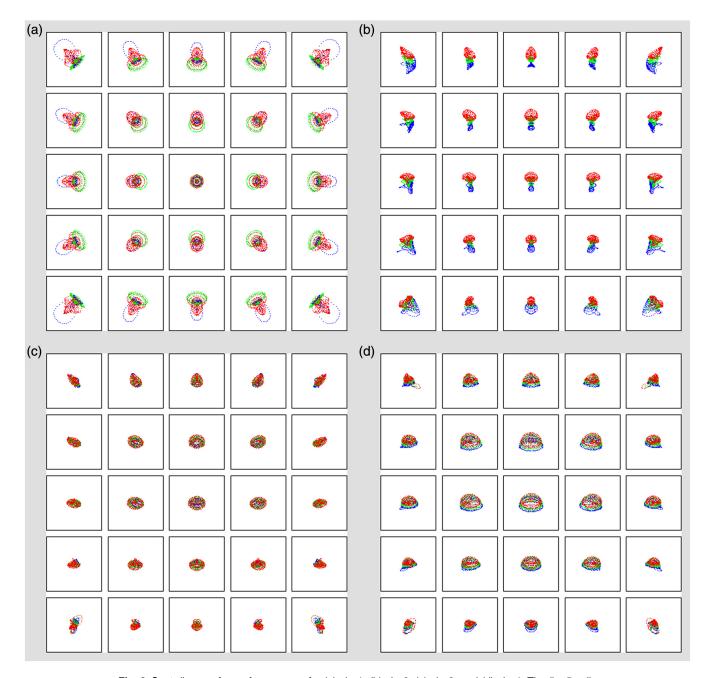
Fig. 3 Spot diagram for on-focus cases for (a) ch. 1, (b) ch. 2, (c) ch. 3, and (d) ch. 4. The 5 × 5 cells represent the FOV of 1 k × 1 k CCD. The size of each cell corresponds to 1 arc sec. Colors indicate simulated images of the shortest (blue), mid (green), and longest (red) wavelength in each channel. Specifically, 400, 470, 550 nm for ch. 1, 550, 630, 700 nm for ch. 2, 700, 760, 820 nm for ch. 3, and 700, 800, 950 nm for ch. 4.

precision transit photometry. The presence of the instrument rotator makes it possible to obtain a potential comparison star located at 1.4 times farther than the length of the side of the field of view. The rotator was designed and manufactured by a limited company, CHUO-OPT, Japan. The rotator is controllable through a serial cable from a Linux-based PC that is attached to MuSCAT2 (the PC also controls the CCD cameras). While the angular resolution of the rotator is 0.89″, the absolute accuracy of pointing a certain position angle is about 0.1 deg, which is limited by the inaccuracy of remounting of the rotator to the telescope (together with MuSCAT2 to exchange instruments) and that of determining origin using a photomicro sensor.

The range of the angle that the rotator can mechanically rotate is ±90 deg; however, it is currently operated in the range of ±45 deg for safety reason. Although the gear train has basically no backlash, it can move a little bit depending on the telescope position due to mechanical flexure, which alters the position of stars on the detectors by up to ∼1″.

4 Commissioning Observations and Results

First-light commissioning of MuSCAT2 was made on August 24 (the night of August 23), 2017 UT. Subsequently, we conducted commissioning observations through 2017 and early 2018. We have examined the performance of MuSCAT on
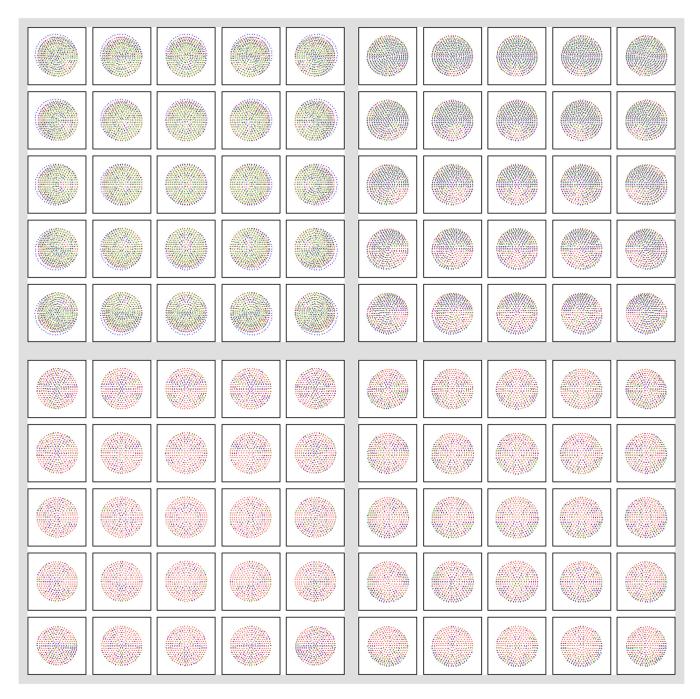
Fig. 4 Same as Fig. 3, but for defocused cases where the secondary mirror is moved by 5 mm from the focused position. In this case, the size of each cell corresponds to 10 arc sec.

Table 1 Sizes and wedge angles of the DMs.

	Height (mm)	Width (mm)	Depth (mm)	Wedge angle (arc min)
DM1	151.87	141.87	15.37	8
DM2	139.87	131.90	15.37	9
DM3	121.88	119.89	15.38	10.9

the TCS 1.52-m telescope. We summarize the results of the commissioning observations below.

4.1 Field of View

We have derived pixel scales and corresponding field of view (FoV) of MuSCAT2 based on images of NGC6885 using TOPCAT[27] and ccmap in IRAF. The derived pixel scales and FoV are 0.44 arc sec per pixel and 7.4×7.4 arc min^2 for all the bands. Thanks to the presence of the instrument rotator, it is possible to obtain a potential comparison star located at
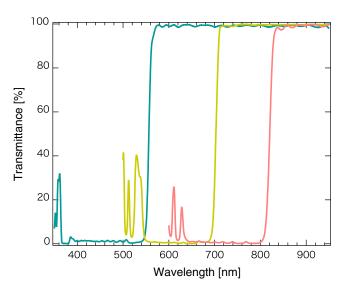
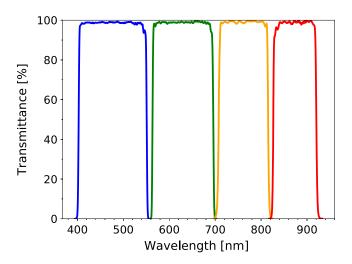**Fig. 5** Transmittance of the DM1 (left, emerald green), DM2 (middle, yellow), and DM3 (right, pink).

Fig. 7 Total transmittance of the MuSCAT2 instrument in g (blue), r (green), i (orange), and z_s (red) bands from left to right.

4.2 Sensitivity and Efficiency

We have estimated zero point magnitudes of MuSCAT2 using the images of M67 as follows. For each band, 300 frames with 2-s exposure were obtained, but seven frames were discarded because they had split PSF due to large guiding feedback during exposure. The remaining 293 frames were bias-subtracted, flat-fielded, position-aligned, and combined into a master image in each band. We then employed SExtractor,[28] ccmap in IRAF, and TOPCAT[27] to identify stars in the master images and to match them with the SDSS DR7 catalog.[29] As a result, we matched about 80 stars in each band. We measured fluxes of the stars and sky background in each band from the master image, and multiplied it by 300/293 to make them correspond to 600-s exposure. The fluxes of the stars and sky background were then converted into magnitudes. The magnitudes of sky background were $g' = 20.4$ mag arc sec^{-2}, $r' = 19.8$ mag arc sec^{-2}, $i' = 19.0$ mag arc sec^{-2}, and $z' = 18.2$ mag arc sec^{-2}, respectively. We fitted relations between MuSCAT2 instrumental magnitudes and the SDSS catalog magnitudes of the stars in each band by a linear function, and derived zero point magnitudes (corresponding to 1 ADU per 600 s) of MuSCAT2 as $g' = 31.56$ mag, $r' = 31.52$ mag, $i' = 30.58$ mag, and $z' = 29.83$ mag, respectively (see Fig. 8). We note that we neglect color terms and simply approximate that the g, r, i, and z_s bands of MuSCAT2 are identical to the SDSS g', r', i', and z' bands.

Fig. 6 Transmittance of g (blue), r (green), i (orange), and z_s (red) bandpass filters from left to right. The gaps of the bandpass filters are coincided with the rises of transmittance shown in Fig. 5.

about 10 arc min away from a target star. We have confirmed that centers of FoV of four CCD cameras are adjusted within 10 pixels in both x and y directions and relative rotations of the position angle fit within 1 deg.
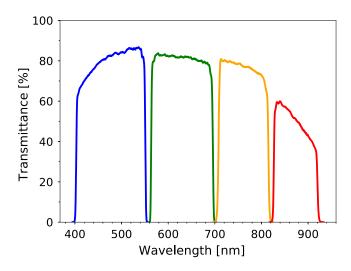
Table 2 Dark current and readout noise of CCDs based on inspection verification by the manufacturer.

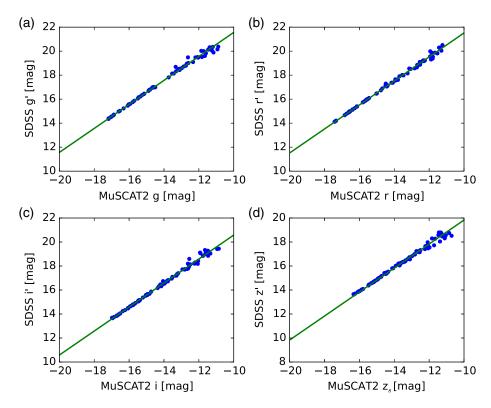| CCD	Band	Dark current (e$^-$ pix^{-1} s^{-1})	Readout noise (100 kHz) (e$^-$ pix^{-1} rms)	Readout noise (2 MHz) (e$^-$ pix^{-1} rms)	Gain (e$^-$ ADU^{-1})
ch.1	g	0.0012	4.08	12.35	1.04
ch.2	r	0.0003	3.96	11.51	0.96
ch.3	i	0.00047	4.02	13.13	1.03
ch.4	z_s	0.00047	4.48	12.56	1.02

Fig. 8 Relations between MuSCAT2 instrumental magnitudes (horizontal) and the SDSS catalog magnitudes (vertical) of the stars for (a) g, (b) r, (c) i, and (d) z_s bands, respectively. Green solid lines represent the best-fit linear functions. Zero point magnitudes are derived as y-intercept of the best-fit functions.

We then calculated ratios of the stellar noise ($n_{stellar}$), the sky noise (n_{sky}), and the readout noise (n_{read}) to the signal using the following equations:

$$n_{stellar}/\text{signal} = [10^{-0.4(m-Z)}]^{0.5}/[10^{-0.4(m-Z)}], \quad (1)$$

$$n_{read}/\text{signal} = n(AN_{exp})^{0.5}/[10^{-0.4(m-Z)}], \quad (2)$$

$$n_{sky}/\text{signal} = [A10^{-0.4(sky-Z)}]^{0.5}/[10^{-0.4(m-Z)}], \quad (3)$$

where m is the MuSCAT2 instrumental magnitude, Z is the zero point magnitude, n is the readout noise in ADU per pixel (see Table 2), A is the area of the aperture (a circle with the radius of 1.7 times of FWHM), N_{exp} is the number of exposures, and sky is the sky background magnitudes. We compute square sum of those noises (total noises) and plot them in Fig. 9. We derive limiting magnitudes of MuSCAT2 giving the signal-to-noise (S/N) ratio of 10 with 10-min exposure as $g'_{lim} = 20.5$ mag, $r'_{lim} = 20.5$ mag, $i'_{lim} = 19.7$ mag, and $z'_{lim} = 19.0$ mag.

Finally, we estimate total throughput (TP) of the TCS 1.52-m telescope and MuSCAT2 by comparing measured fluxes coming from stars with expected fluxes from known magnitudes. The measured total TP values are 26%, 33%, 22%, and 15%, respectively, for in g, r, i, and z_s bands. We also estimate expected total TP as shown in Table 3, considering transmittance of sky, reflectivity of the primary and secondary mirrors, transmittance and reflectivity of MuSCAT2 optics (including lens, mirror, DMs, and filters), and quantum efficiency (QE) of detectors with broadband antireflection (BBAR) coating on the camera window. To calculate the sky transmittance, we employ the libRadtran software package[30] to model the telluric atmosphere with aerosol at the elevation of 2390 m. Since the aerosol model is not definitive but has large uncertainty, the expected TP has uncertainties of several percent. We also note that we neglect the effect of spiders, which would cause an additional few percent loss of light. Consequently, we found that the TP in g and r bands are roughly in agreement with the expected ones, but that in i band is a bit lower and that in z_s band is significantly worse than expected. Although an exact reason is uncertain, we suspect that this is due to degradation of reflectivity of the primary and secondary mirrors due to micron-sized dusts on surfaces of them.

4.3 CCD Nonlinearity

We have examined the linearity and saturation level of the individual CCDs by taking dome flat images with various exposure times. The illumination source of the dome flat is composed of two types of lamps, one is a fluorescent lamp and the other is a voltage-controllable filament lamp, both distributed on the wall. Because the illuminance of these lamps is not stable but time variable, we have taken the following procedure to mitigate this effect. First, for each CCD, we adjusted the voltage of the filament lamps so that the average count of a flat image with the exposure time of 10 s became about 30,000 ADU. Second, we obtained a set of dome-flat images with a range of exposure times from 1 s through 23 s, with which most of the pixels are saturated, being incremented by 1 s. In addition to those "experimental" data, we also took "reference" images with the exposure time of 10 s in between two consecutive
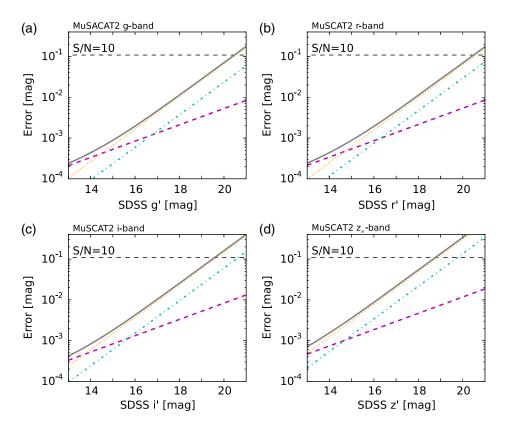
Fig. 9 Relations of SDSS magnitudes (horizontal) and expected errors for 600 s in magnitude (vertical) for (a) g, (b) r, (c) i, and (d) z_s bands, respectively. Black solid, magenta dashed, orange dotted, and aqua dot-dashed lines represent total noise, stellar noise, readout noise, and sky noise, respectively.

Table 3 Summary of TP of MuSCAT2 on the TCS 1.52-m telescope.

Band	Sky transmittance (%)	M1 (%)	M2 (%)	MuSCAT2 (Total) (%)	Expected TP (%)	Measured TP (%)
g	81[a]	70[b]	70[b]	80	32	26
r	89[a]	70[b]	70[b]	81	35	33
i	92[a]	70[b]	70[b]	77	35	22
z_s	95[a]	70[b]	70[b]	51	24	15

Notes: M1 = primary mirror, M2 = secondary mirror, MuSCAT2 (total) = all optics including filters, CCD QE, and BBAR coating.
[a]Based on a model atmosphere by the libRadtran software package.[30]
[b]Assumed.

experimental exposures. We repeated this set of exposures three times for each CCD.

After subtracting a dark image from all of the exposed images, we have calculated average counts on the individual exposed images. Then, for each experimental image we have estimated the expected count by multiplying the average count of the adjacent reference images by $t_{exp}/10$, where t_{exp} is the exposure time of an experimental image in seconds. In Fig. 10, we show the ratio of the measured average count to the expected one calculated for the experimental images as a function of the measured count for the respective CCDs. In all plots, the measured-to-expected ratio is distributed around unity up to 62,000 to 64,000 ADU, above which the value drops due to saturation. Below the saturation level, the measured-to-expected ratio gradually decreases with the measured

count. We fit the data below 62,000 ADU with a linear function, which gives the following relations:

$$y = -0.00085x + 1.00283 (\text{ch.1}), \qquad (4)$$

$$y = -0.00098x + 1.00328 (\text{ch.2}), \qquad (5)$$

$$y = -0.00129x + 1.00435 (\text{ch.3}), \qquad (6)$$

$$y = -0.00164x + 1.00563 (\text{ch.4}), \qquad (7)$$

where x and y are the measured count $\times 10^{-4}$ (ADU) and the measured-to-expected ratio, respectively. The best-fit models
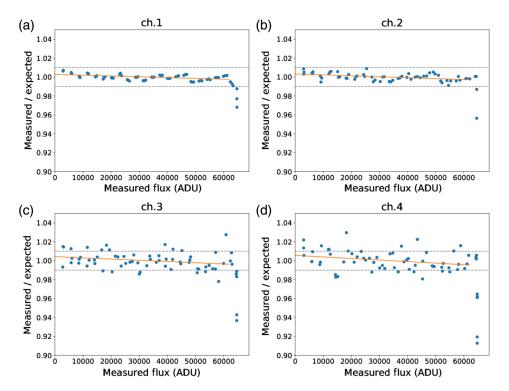
Fig. 10 Relations of measured fluxes (horizontal) and ratios of measured fluxes to expected ones (vertical) for CCD cameras for (a) g, (b) r, (c) i, and (d) z_s bands, respectively. The orange solid lines represent the best-fit linear function models. The gray dotted lines indicate boundaries of 1% nonlinearity.

are plotted by an orange solid line in Fig. 10. These results indicate that the nonlinearity of all the CCDs are well below 1% up to ~62,000 ADU. According to Mann et al.,[31] the effect of CCD non-linearity on photometric precision can be written as, rms $\sim \sqrt{2}\alpha\sigma^2/\sqrt{N}$, where α is the level of nonlinearity in the pertinent ADU range, σ is the standard deviation of normalized incident flux, and N is the number of pixels in an aperture of interest. In our observation, N is typically 300 to 1000. If we assume $= 0.01$ (the nonlinearity level of 1%) and a conservative atmospheric condition of $f = 0.3$ (incident flux varies by 30% rms), the photometric noise arising from the CCD nonlinearity is <0.008%. Therefore, the CCD nonlinearity up to 62,000 ADU is basically negligible for transit photometry with MuSCAT2.

4.4 Self Auto-Guiding and Correction of Periodic Tracking Error

Tracking accuracy of the TCS is not very good such that telescope pointing drifts up to ~1′ per hour without any guiding (see Fig. 11). Auto guiding is thus essential both to keep the target and comparison stars within the same field of view for a whole night and to fix the stellar positions within several pixels to minimize systematic errors in photometry arising from inter-pixel sensitivity variations.

Since MuSCAT2 itself has neither on-axis nor off-axis guiding camera, we adopt a self autoguiding system, that is, science images taken by the instrument itself are used for guiding. We implement a self autoguiding software, the original version of which was developed for MuSCAT at Okayama.[15] The software calculates the stellar positional shifts between the latest science image and a reference image in one of the four channels

immediately, and soon feeds it back to the telescope to correct the telescope position. Note that in the original software the stellar positional shifts are calculated using the centroids of several bright stars, whereas this time we have introduced a different algorithm in which one-dimensional cross correlations in both X and Y directions are calculated between the two images, and the shifts are calculated so as to minimize the cross correlations. This algorithm is more robust in the events of cloud passing and for stellar crowded fields. The algorithm works for both on-focus and defocused observations. The time lag between the observation of the latest image and the time that the correction signal is sent to the telescope is $\sim 3 - 6 + 0.5 \times T_{exp}$s, where T_{exp} is the exposure time of the current image. To avoid over correction, the guiding frequency is usually set at once in 30 to 60 s. The channel to be used for guiding is user-selectable, but usually r- or i-band channel is selected to minimize the effect of differential atmospheric refraction, which causes a gradual positional shift of stars on a different-band channel depending on the airmass.

Figure 11 shows a sample of time variations of stellar position with (middle panel) and without (top panel) the self auto-guiding software. With guiding, long-term trends of positional shifts are significantly suppressed. On the other hand, stellar positions also exhibit a periodic variation in the RA direction with the period of ~169 s and the semiamplitude of ~3 to 6 pixels (depending on declination), which cannot be corrected by the self autoguiding function because of its high frequency. Even with this periodic drift, the systematic noises in photometry arising from the interpixel sensitivity variations can well be suppressed by applying Gaussian process (see Sec. 4.5). However, this periodic motion also makes a stellar PSF significantly elongated when the exposure time is longer
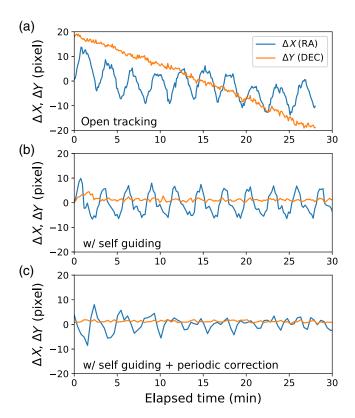
Fig. 11 Sample data of stellar positions on a CCD as a function of time. The X (RA) and Y (DEC) positions are shown in orange and blue, respectively. (a) The data taken without any guiding and correction. (b) The data taken with the self auto guiding activated. (c) The data taken with both the self guiding and periodic correction for tracking applied. Note that these three datasets were taken on different nights for different targets. The declinations of the targets were 0, 0, and −11 deg for the top, middle, and bottom datasets, respectively.

than ∼5 s, which makes it difficult to observe faint objects or crowded fields with a long exposure time.

The cause of this periodic error could be attributed to inhomogeneity of gears in the gear train that drives the RA axis of TCS. Tracking a sidereal object with TCS is achieved by driving a motor for the RA axis, attached to the end of the gear train, at a constant period that corresponds to the sidereal motion. Therefore, any inhomogeneity in one or more of the gears results in periodic acceleration and deceleration in the telescope motion.

The ultimate solution for this problem would be to renovate the telescope control system by attaching a high-resolution encoder directly to the RA axis and by controlling the motor speed by referring to the encoder value. However, it would be very costly and time-consuming. Alternatively, as a tentative solution, we have added a function to the telescope control system that can sinusoidally accelerate and decelerate the motor speed so as to cancel out the tracking error. In this function, a velocity of the telescope V_{new}, which is the velocity that is intended to be driven by the motor on the assumption that the gear train has no error, is given by the following formulas:

$$V_{new} = V_{sidereal} + \delta V, \tag{8}$$

$$\delta V = A \sin(Bx + C) + D, \tag{9}$$

where $V_{sidereal}$ is the sidereal speed ($15'' s^{-1}$), x is the hour angle of a tracking object, and A, B, C, and D are the coefficients.

To decide how to determine the values of coefficients, we have investigated the behavior of the periodic error and found that (1) the period is almost constant (∼169 s) over all telescope positions, (2) the period and/or the phase are slightly variable depending on hour angle, and (3) the amplitude does not depend on hour angle but on declination. Due to the complexity of the features (2) and (3), it is difficult to predict the values of coefficients beforehand with sufficient precisions. Instead, we have decided to determine or refine the coefficients during observations. Specifically, in each observation, for the first 5 min the target is observed without correcting the periodic error (but with the self guiding function activated) to gather the data of periodicity. Subsequently, the initial values of A, C, and D are determined by fitting the stellar positional data in the RA direction gathered in the initial phase, whereas B is fixed at a typical value. After applying the periodic correction to the telescope tracking, the values of B, C, and D are re-evaluated every 6 min using the positional data of the last 6 min, where the value of A is fixed at the initial value.

The bottom panel of Fig. 11 shows a sample of stellar positional data with the periodic correction applied. In this figure, the initial learning phase started at the time of zero, and the periodic correction function was applied 5 min later. Note that the self autoguiding function was also activated during this observation. As can be seen, the dispersion of stellar position in the RA direction was gradually suppressed after the periodic correction was applied, which finally stabilized at the level of ∼1.8 pixels in rms.

4.5 Demonstration of High Precision Transit Photometry

To test achievable photometric precision, we observed a full-transit of WASP-12b on January 25, 2018. WASP-12 is a G0 dwarf with $V = 11.57 \pm 0.16$ mag based on the Tycho-2 catalog.[32] WASP-12 was observed from 20:46 of January 25 to 02:43 of January 26 in UT (airmass: 1.2–1.0–1.4). Exposure times and numbers of exposures for each band are summarized in Table 4. Stellar images were defocused to avoid saturation of a brighter comparison star. We note that because the software of correcting periodic tracking error was under development at the time of this observation, only the self auto-guiding software was activated to correct tracking error.

The photometry is calculated using a Python-based photometry pipeline specially developed for MuSCAT2. The pipeline

Table 4 Summary of the test observation and analysis.

Target	Band	Exp. time (s)	N_{data}[a]	F_c/F_t[b]	R_{ap}[c] (pix)
WASP-12	g	10	1863	2.8	16
WASP-12	r	6	2850	2.8	12
WASP-12	i	20	920	2.9	16
WASP-12	z_s	45	462	3.1	16

[a]Numbers of observed data points.
[b]Unnormalized flux ratios of the target star and ensembles of comparison stars.
[c]Applied aperture radii.

first computes the astrometric solution for each image frame using an offline version of astrometry.net,[33] and then calculates the photometry (carrying out the basic data reductions, such as flat field division and bias subtraction) for the target and comparison stars for a set of aperture size. The pipeline also calculates the usual set of covariates, such as star centroids, background sky level, airmass, etc. for each image frame to be used later in detrending. The pipeline is optimised for defocused photometry, and calculates aperture entropy as a proxy to the PSF FWHM, which can be used in the detrending instead of the FWHM. The aperture entropy is calculated as, $E = -\sum_i F_i \log F_i$, where F is the fluxes inside the photometry aperture normalized by the total aperture flux (that is, we calculate the entropy of the flux distribution). We also derive the effective FWHMs by calculating a table of aperture entropies for a set of Gaussian PSFs with varying FWHM values for all the aperture size and use the table to map the entropies to FWHMs.

The light curves are detrended and modeled in two steps. First, a set of optimal apertures are chosen to minimize the relative light curve point-to-point scatter, and a transit model computed using PyTransit[34] is fitted together with a linear baseline model with the centroid x- and y-shifts (dx and dy), sky level, airmass, and aperture entropy as covariates. The fitting is carried out using the light curves for the four filters jointly to minimize the sensitivity to systematics not explained by the covariates. As a final step, we model the light curve as a sum of a transit signal and systematics represented as a Gaussian process (GP).[35–37] The GP uses the same covariates as the linear model, and its hyperparameters are learned from the data by fitting a GP to the light curves with the best-fitting transit model removed. We use a transit model with quadratic limb darkening coefficients. The limb darkening coefficients are free with uninformative priors so that the parameter estimates are

marginalized over all limb darkening profiles allowed by the observations. Finally, the transit model parameter posteriors are estimated by Markov chain Monte Carlo (MCMC) sampling using the GP to represent the systematics. Normalized transit light curves, best-fit detrending + transit light curve models based on the MCMC sampling, and their residuals are plotted in Fig. 12, and detrended transit light curves overlaid with the best-fit transit light curve models are shown in Fig. 13.

We calculate rms of residuals per 1 min for each band, and derived ones are 0.057%, 0.050%, 0.060%, and 0.076%, respectively for g, r, i, and z_s bands. To understand how photometric performance is achieved, we roughly estimate error budgets for this observation as shown in Table 5. In the table, σ_{target}, σ_{comp}, and σ_{sky} indicate typical photon noises (Poisson noises) per 1 min arising from fluxes of the target, comparison stars, and sky-background, respectively. σ_{read} is a noise caused by the readout noise (see Table 2) within the aperture. Finally, σ_{expected} is a total expected noise per 1 min, which is calculated by the square root of the sum of the squares of above noises. The values of σ_{expected} and rms are in good agreement, meaning the observed photometric precision can be mostly explained by photon noises of the target, comparison stars, and sky-background noises and additional readout noise of the CCDs. The slightly larger rms than σ_{expected} in g and r bands may be due to a scintillation noise caused by the short exposure times in those bands. Finally, to evaluate a possible error caused by telescope guiding, we have also tried to fit the light curves without using dx and dy as covariates. We find that the total rms values become larger by ∼0.02% in all the bands. This means that centroid shifts may cause a potential error of ∼0.05% to 0.06% unless properly decorrelated. We also note that transit parameters of the WASP-12b data will be presented in a separated paper.[38]
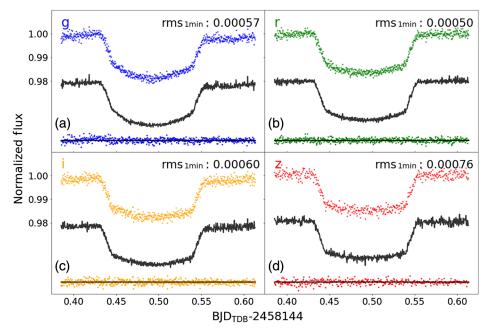

Fig. 12 Transit light curves of WASP-12b taken on January 25, 2018, for (a) *g*, (b) *r*, (c) *i*, and (d) *z_s* bands, respectively. The black solid lines indicate best-fit detrending+transit models. The best-fit models and residuals of the data from the best-fit models are shifted for visual purposes. Root-mean-square values of residuals with 1-min binning are shown in upper-right corner of each panel.
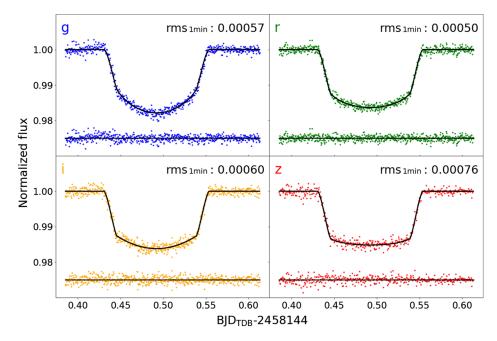
Fig. 13 Same as Fig. 12, but for detrended light curves. The overlaid black solid lines indicate the best-fit transit models.

Table 5 Rough estimates of error budgets per 1 min.

Target	Band	σ_{target} (%)	σ_{comp} (%)	σ_{sky} (%)	σ_{read} (%)	$\sigma_{expected}$ (%)	$rms_{1\ min}$ (%)
WASP-12	g	0.039	0.025	0.016	0.012	0.051	0.057
WASP-12	r	0.034	0.021	0.010	0.008	0.043	0.050
WASP-12	i	0.049	0.030	0.020	0.014	0.063	0.060
WASP-12	z_s	0.062	0.037	0.031	0.016	0.081	0.076

4.6 Discussion

The demonstrated results can be compared with the photometric performance of MuSCAT, which is mounted on the Okayama 1.88-m telescope. WASP-12 was also observed with MuSCAT as a demonstration of photometric precision in Narita et al.,[15] in which the photometric precision per 1 min was 0.12%, 0.12%, and 0.15% in g, r, and z_s bands, respectively. Although one of the dominant noise sources in the MuSCAT observation was sky background, another dominant source was unknown (unpredictable) systematics, probably arising from telluric atmosphere (e.g., the second-order extinction[16]). As a result, the photometric precisions were twice as bad than those achieved here with MuSCAT2, although the expected photon noises from the target star are comparable in both cases. As described above, the photometric noises observed with MuSCAT2 can well be explained by known (predictable) noise sources, and no systematic noise is apparent under favor of the higher elevation of the Teide observatory (2390 m) than the Okayama observatory (372 m).

Based on the photometric performance of MuSCAT achieved for HAT-P-14, Fukui et al.[16] demonstrated that MuSCAT has an ability to probe the atmospheres of transiting planets as small as a super-Earth/mini-Neptune ($\sim 2.5 R_\oplus$) around a nearby

M dwarf. Comparing with this result, MuSCAT2 should have a similar, or even better, ability to probe the atmosphere of exoplanets thanks to the better photometric precision and the presence of an extra channel (i band).

Multicolor transit photometry, combined with a physically-based light contamination model and Bayesian analysis framework, can be also used to estimate the true radius ratio of the transiting object, which allows us to distinguish planetary-size objects from stellar-size objects. The foundations of this approach have been laid out in previous studies,[39–41] and the full Bayesian approach will be detailed in Parviainen et al. in prep. MuSCAT2 will become one of the best instruments in the world for the purpose to discriminate whether candidates of transiting planets are real planets or false positives due to eclipsing binaries.

We finally note how we determine a degree of defocusing and an exposure time for each target. The optimal image size basically depends on the brightness of the target and/or comparison stars and the dead time of the detector. In the case of bright stars ($\lesssim 14$ mag), sky background noise is negligible even with moderate defocusing, whereas faint stars ($\gtrsim 15$ mag) are sensitive to sky background, which makes focused observation essential. On the other hand, CCD cameras have finite dead time (1 to 4 s), which makes observation with a short exposure

time that is comparable to the dead time inefficient. Therefore we usually set the exposure time at 15 s or longer for any targets except for very bright targets, and adjust the defocused size so that the target and comparison stars will not saturate with the given exposure time.

5 Summary

We have developed an astronomical instrument MuSCAT2 for the TCS 1.52 m telescope in the Teide observatory, Tenerife, Spain. MuSCAT2 has a capability of four-color simultaneous imaging in g (400 to 550 nm), r (550 to 700 nm), i (700 to 820 nm), and z_s (820 to 920 nm) bands with four $1 k \times 1 k$ pixel CCDs. The field of view of MuSCAT2 is 7.4×7.4 arc min^2 with the pixel scale of 0.44 arc sec per pixel.

As shown in Sec. 4.5, MuSCAT2 is able to achieve well better precision than 0.1% for a G0V star with V $\sim$ 11.6. The capability of demonstrated high photometric precision and four-color simultaneous imaging would be useful to confirm whether candidates of transiting planets discovered by transit surveys are true planets or false positives due to eclipsing binaries. This is especially powerful in the TESS and PLATO era, which will produce thousands of candidates in upcoming years. MuSCAT2 has started science operations since January 2018, and over 250 nights per year will be allocated for the MuSCAT2 consortium at least until 2022. MuSCAT2 will substantially contribute to follow-up transit observations of the TESS and PLATO space missions.

Acknowledgments

References

1. G. Á. Bakos et al., "HAT-P-1b: a large-radius, low-density exoplanet transiting one member of a stellar binary," *Astrophys. J.* **656**, 552–559 (2007).
2. A. C. Cameron et al., "WASP-1b and WASP-2b: two new transiting exoplanets detected with SuperWASP and SOPHIE," *Mon. Not. R. Astron. Soc.* **375**, 951–957 (2007).
3. R. J. Siverd et al., "KELT-1b: a strongly irradiated, highly inflated, short period, 27 jupiter-mass companion transiting a mid-F star," *Astrophys. J.* **761**, 123 (2012).
4. D. Charbonneau et al., "A super-Earth transiting a nearby low-mass star," *Nature* **462**, 891–894 (2009).
5. M. Gillon et al., "Temperate Earth-sized planets transiting a nearby ultracool dwarf star," *Nature* **533**, 221–224 (2016).
6. P. J. Wheatley et al., "The next generation transit survey (NGTS)," *Mon. Not. R. Astron. Soc.* **475**, 4476–4493 (2018).
7. A. Baglin et al., "CoRoT: a high precision photometer for stellar ecolution and exoplanet finding," in *36th COSPAR Scientific Assembly, COSPAR, Plenary Meeting*, Vol. 36, p. 3749 (2006).
8. W. J. Borucki et al., "Kepler planet-detection mission: introduction and first results," *Science* **327**, 977–980 (2010).
9. S. B. Howell et al., "The K2 mission: characterization and early results," *Publ. Astron. Soc. Pac.* **126**, 398–408 (2014).
10. G. R. Ricker et al., "Transiting exoplanet survey satellite (TESS)," *J. Astron. Telesc. Instrum. Syst.* **1**(1), 014003 (2015).
11. H. Rauer et al., "The PLATO 2.0 mission," *Exp. Astron.* **38**, 249–330 (2014).
12. K. A. Collins et al., "The KELT follow-up network and transit false positive catalog: pre-vetted false positives for TESS," *Astron. J.* **156**, 234 (2018).
13. A. Santerne et al., "SOPHIE velocimetry of Kepler transit candidates. VII. A false-positive rate of 35% for Kepler close-in giant candidates," *Astron. Astrophys.* **545**, A76 (2012).
14. P. W. Sullivan et al., "The transiting exoplanet survey satellite: simulations of planet detections and astrophysical false positives," *Astrophys. J.* **809**, 77 (2015).
15. N. Narita et al., "MuSCAT: a multicolor simultaneous camera for studying atmospheres of transiting exoplanets," *J. Astron. Telesc. Instrum. Syst.* **1**, 045001 (2015).
16. A. Fukui et al., "Demonstrating high-precision, multiband transit photometry with MuSCAT: A Case for HAT-P-14b," *Astrophys. J.* **819**, 27 (2016).
17. N. Narita et al., "The K2-ESPRINT project. VI. K2-105 b, a hot Neptune around a metal-rich G-dwarf," *Publ. Astron. Soc. Jpn.* **69**, 29 (2017).
18. B. S. Gaudi et al., "A giant planet undergoing extreme-ultraviolet irradiation by its hot massive-star host," *Nature* **546**, 514–518 (2017).
19. T. Hirano et al., "Exoplanets around low-mass stars unveiled by K2," *Astron. J.* **155**, 127 (2018).
20. A. Fukui et al., "Ground-based transit observation of the habitable-zone super-earth K2-3d," *Astron. J.* **152**, 171 (2016).
21. D. J. Armstrong et al., "One of the closest exoplanet pairs to the 3:2 mean motion resonance: K2-19b and c," *Astron. Astrophys.* **582**, A33 (2015).
22. N. Narita et al., "Characterization of the K2-19 multiple-transiting planetary system via high-dispersion spectroscopy, AO imaging, and transit timing variations," *Astrophys. J.* **815**, 47 (2015).
23. A. Fukui et al., "Optical-to-near-infrared simultaneous observations for the hot uranus GJ3470b: a hint of a cloud-free atmosphere," *Astrophys. J.* **770**, 95 (2013).
24. H. Parviainen et al., "The GTC exoplanet transit spectroscopy survey. II. An overly large Rayleigh-like feature for exoplanet TrES-3b," *Astron. Astrophys.* **585**, A114 (2016).
25. Y. Kawashima and M. Ikoma, "Theoretical transmission spectra of exoplanet atmospheres with hydrocarbon haze: effect of creation, growth, and settling of haze particles. I. Model description and first results," *Astrophys. J.* **853**, 7 (2018).
26. A. Oscoz and M. Monelli, "Telescopio Carlos Sánchez," 2016, http://www.iac.es/OOCC/instrumentation/telescopio-carlos-sanchez/ (26 November 2018).
27. M. B. Taylor, "TOPCAT STIL: starlink table/VOTable processing software," in *Astronomical Data Analysis Software and Systems XIV*, Astronomical Society of the Pacific Conference Series, P. Shopbell, M. Britton, and R. Ebert, Eds., vol. **347**, p. 29 (2005).
28. E. Bertin and S. Arnouts, "SExtractor: software for source extraction," *Astron. Astrophys. Suppl.* **117**, 393–404 (1996).
29. K. N. Abazajian et al., "The seventh data release of the Sloan digital sky survey," *Astrophys. J. Suppl.* **182**, 543–558 (2009).
30. B. Mayer and A. Kylling, "Technical note: the libRadtran software package for radiative transfer calculations—description and examples of use," *Atmos. Chem. Phys.* **5**, 1855–1877 (2005).
31. A. W. Mann, E. Gaidos, and G. Aldering, "Ground-based submillimagnitude CCD photometry of bright stars using snapshot observations," *Publ. Astron. Soc. Pac.* **123**, 1273–1289 (2011).
32. E. Høg et al., "The Tycho-2 catalogue of the 2.5 million brightest stars," *Astron. Astrophys.* **355**, L27–L30 (2000).
33. D. Lang et al., "Astrometry.net: blind astrometric calibration of arbitrary astronomical images," *Astron. J.* **139**, 1782–1800 (2010).
34. H. Parviainen, "PYTRANSIT: fast and easy exoplanet transit modelling in PYTHON," *Mon. Not. R. Astron. Soc.* **450**, 3233–3238 (2015).
35. C. E. Rasmussen and C. Williams, *Gaussian Processes for Machine Learning*, The MIT Press, Cambridge, Massachusetts (2006).
36. N. P. Gibson et al., "A Gaussian process framework for modelling instrumental systematics: application to transmission spectroscopy," *Mon. Not. R. Astron. Soc.* **419**, 2683–2694 (2012).

37. S. Ambikasaran et al., "Fast direct methods for Gaussian processes," *IEEE Trans. Pattern Anal. Mach. Intell.* **38**(2), 252–265 (2016).

38. Parviainen et al., "Multi-colour photometry of exoplanet transits in exoplanet candidate validation," *A&A* to be submitted.

39. F. Rosenblatt, "A two-color photometric method for detection of extra solar planetary systems," *Icarus* **14**, 71–93 (1971).

40. A. J. Drake, "On the selection of photometric planetary transits," *Astrophys. J.* **589**, 1020–1026 (2003).

41. B. Tingley, "Using color photometry to separate transiting exoplanets from false positives," *Astron. Astrophys.* **425**, 1125–1131 (2004).

Norio Narita is the PI of the MuSCAT/MuSCAT2 instruments and its observing team. He is an assistant professor of the University of Tokyo and concurrently working as a JST PRESTO researcher.

Biographies of the other authors are not available.